https://doi.org/10.5194/egusphere-2022-714
Preprint. Discussion started: 12 September 2022
© Author(s) 2022. CC BY 4.0 License.

Modeling the Inhibition Effect of Straw Checkerboard Barriers on Wind-blown Sand

Haojie Huang[1,2,3]

[1]School of Energy and Power Engineering, University of Shanghai for Science and Technology, Shanghai, PR China

[2]MOE Engineering Research Center of Desertification and Blown-sand Control, Beijing Normal University, Beijing, PR China

[3]College of Mechanics and Materials, Hohai University, Nanjing, Jiangsu 211000, PR China

Correspondence: H.J. Huang (hjhuang@usst.edu.cn)

Abstract

Straw checkerboard barriers (SCBs) are usually laid to prevent or delay the process of desertification caused by aeolian sand erosion in arid and semi-arid regions. Understanding the impact of SCBs and its laying length on aeolian sand erosion is of great significance to reduce the damage and the laying costs. In this study, a three-dimensional wind-blown sand model in presence of SCBs was established by introducing the splash process and equivalent sand barriers into a large-eddy simulation airflow. From this model, the inhibition effect of SCBs on wind-blown sand was studied qualitatively, and the sensitivity of aeolian sand erosion to the laying length was investigated. The results showed that the wind speed in the SCBs area decreases oscillatively along the flow direction. Moreover, the longer the laying lengths, the lower the wind speed in the stable stage behind SCBs, and the lower the

https://doi.org/10.5194/egusphere-2022-714
Preprint. Discussion started: 12 September 2022
© Author(s) 2022. CC BY 4.0 License.

sand transport rate. We further found that the concentration of sand particles near the side of SCBs is higher than that in its central region, which is qualitatively consistent with the previous research. Our results also indicated that whether the wind speed will decrease below the impact threshold or the fluid threshold is the key factor affecting whether sand particles can penetrate the SCBs and form stable wind-blown sand behind the SCBs under the same conditions. Our research can provide theoretical support for the minimum laying length of SCBs in anti-desertification projects.

1. Introduction

In arid and semi-arid areas, aeolian sand erosion is becoming more and more serious. How to prevent or delay the process of desertification is a major challenge for all over the world, especially in the transitional areas between desert and oasis. At present, shelterbelt (Wang et al., 2010), sand fences (Bitog et al., 2009; Hatanaka and Hotta, 1997; Li and Sherman (2015); Lima et al., 2017; Pye and Tsoar, 2008; Wilson, 2004), wind-break walls (Bouvet et al., 2006; Santiago et al., 2007), hole plate-type sand barriers (Chen et al., 2019) and straw checkerboard sand barriers (Bo et al., 2015; Huang et al., 2013; Wang and Zheng, 2002; Xu et al., 2018) are the main techniques to prevent the process of desertification. Among these techniques, straw checkerboard barriers (SCBs) are the most common used in the anti-desertification projects because of their advantages of easy to obtain and relatively cheap (Zheng, 2009). Laying SCBs could play an important role in the ecological restoration of sandy land ecosystems (Zhang et al., 2018) and vegetation restoration. Some research showed that the SCBs can effectively reduce the surface wind speed (Qu et al., 2007), increase

https://doi.org/10.5194/egusphere-2022-714
Preprint. Discussion started: 12 September 2022
© Author(s) 2022. CC BY 4.0 License.

the surface roughness (Zhang et al., 2016), weaken the sand transport rate (Bo et al., 2015), change the distribution of aeolian sandy soil particles and soil organic carbon (Dai et al., 2019), thus protecting the survival of the vegetation and achieving sustainable development of oasis and ecological environment.

In recent decades, SCBs have been widely used in northwest of China, which is seriously damaged by aeolian sand erosion. For example, the SCBs have been laid on the sides of the roadbed along the railways such as Baotou-Lanzhou Railway, Wuda-Jilantai Railway (Wang, 1996), Gantang-Wuwei Railway (Yang, 1995), Lanzhou-Xinjiang Railway (Binwen et al., 1998; Cheng et al., 2016), Qinghai-Tibet Railway (Cheng and Xue, 2014; Zhang et al., 2010), as well as the windy sand area beside the desert roads such as Taklamakan Desert Highway (Li et al., 2006; Qu et al., 2007), Tarim Desert Highway (Xu et al., 1998) and MinQin Desert Highway. In addition, SCBs are adopted by some countries that are also affected by aeolian sand erosion, such as Ghana, Egypt, and Iran (Zheng, 2009). Although the SCBs have been widely used, its design size and laying methods are mainly determined by practical experience or repeated tests. For example, for the sand fence which has the similar effect to the SCB, Li and Sherman (2015) combined experimental and field data to conclude that the optimal design of sand fence is closely related to its aerodynamics and morphodynamics. The effect of sand fences with different porosity, spacing and height on the wind field is significant (Lima et al., 2017; Lima et al., 2020). However, the complexity of the flow field around the SCBs and the movement of sand particles, as well as the coupling of particles and flow field, which makes this problem more

https://doi.org/10.5194/egusphere-2022-714
Preprint. Discussion started: 12 September 2022
© Author(s) 2022. CC BY 4.0 License.

difficult. Therefore, it is necessary to study the characteristics of turbulence inside and behind the SCBs as well as the influence mechanism of the laying length on wind speed and erosion.

Wang and Zheng (2002) proposed a single-row ideally uniformly distributed vortex model to simplify the flow field of the wind-blown sand. Based on their model, the corresponding relationship between the side length and the height of a single SCB was analyzed. Their theoretical results are similar to the size of the SCBs which laid in the Tarim Desert Highway (1 m in side length and 15-20 cm in height). Qiu et al. (2004) pointed out that since the concentration of wind-blown sand below 10 cm near the surface is relatively high, the height of the SCBs should be designed as 10-20cm thus to effectively prevent aeolian sand erosion. The experimental results of Zhang et al. (2018) indicated that the SCB has the best protective effect when its side length is 1 m. These works are of great help to the design of a single SCB. Based on these empirical sizes of the SCBs, researchers tried to analyze the effect of SCBs on the flow field and particles from the perspective of turbulence. Huang et al. (2013) used two-dimensional large eddy simulation and discrete particle tracking methods to simulate the wind-blown sand movement inside the simplified two-dimensional SCBs. The effect of SCBs on surface wind speed was analyzed. They found that sand particles could be aggregated at the inner walls of the SCBs due to the influence of the vortex or the backflow. And then a v-shaped sand trough was formed, which is similar to the actual situation. Bo et al. (2015) equated the SCBs to the source term of the standard k-ε turbulence model, and analyzed the influence of SCBs on the wind speed

https://doi.org/10.5194/egusphere-2022-714
Preprint. Discussion started: 12 September 2022
© Author(s) 2022. CC BY 4.0 License.

profile in two-dimensional flow field without sand particles. They divided the streamwise velocity profile in flow field containing SCBs into three different log-linear functions approximately, and obtained the relationship between them and friction wind speeds. Although these two-dimensional models can reflect the effect of the SCBs on the flow field to some extent, they are far from the real turbulence. Moreover, since the actual three-dimensional SCB is simplified into two-dimensional plane with only streamwise direction and vertical direction. And the impact of this simplification is uncertain. For this reason, Xu et al. (2018) simulated the wind-blown sand movement on the SCBs surface under three-dimensional flow field with OpenFOAM, and mainly analyzed the influence of the flow field inside the SCBs on the movement of sand particles. They concluded that the wind vortex is the main cause of internal morphology of the straw checkerboard. They found that the vortex will drive particles inside the SCBs move towards the front and side walls, making the erosional form in SCB cells become low in the middle and high near all sides. However, the SCBs are completely equivalent to the solid as the bottom boundary condition in their model. As a non-solid material, the SCBs can be penetrated by the wind in practice. It only weakens the wind speed thus not equivalent to a solid. For example, Dupont et al. (2014) equated the surface vegetation to a resistance force through the resistance coefficient and leaf area coefficient, that is, the wind will be resisted as it passes through these equivalent regions.

In order to reasonably introduce the SCBs and consider the coupling among turbulence, SCBs and surface splash process, the development of three-dimensional

https://doi.org/10.5194/egusphere-2022-714
Preprint. Discussion started: 12 September 2022
© Author(s) 2022. CC BY 4.0 License.

model is required. In this paper, three-dimensional numerical coupled model of wind-blown sand in presence of SCBs was carried out to study the inhibition effect of the laying length on aeolian sand erosion. The large eddy simulation approach was used to simulate the clean air flow with the saltation process was considered. Furthermore, we added a volume drag force into the Navier-Stokes equations by using the drag source method to realize the coupling between the SCBs and the wind-blown sand movement. Section 2 and Section 3 gave the three-dimensional numerical coupled model and its validation, respectively. In Section 4, the effects of the SCBs' laying length on clean air flow and sand-laden flow under different friction wind speeds were studied. Finally, Section 5 was a summary of the main conclusions.

2. Models

The Advanced Regional Prediction System (ARPS) has been widely used to simulate turbulent boundary-layer particle-laden flow, such as: wind-blown sand (Dupont et al., 2013; Huang, 2020), wind-blown snow (Huang and Wang, 2016; Li et al., 2018). The standard version of the program is described in the ARPS User's Manual (Xue et al., 1995) and its validation cases are referred to Xue et al. (2000) and Xue et al. (2001). For this study, some suitable models were added in order to simulate turbulent boundary-layer flow in presence of SCBs with saltating sand particles. A detailed description of these modifications is shown in the following subsections.

2.1 Turbulent boundary-layer flow

https://doi.org/10.5194/egusphere-2022-714
Preprint. Discussion started: 12 September 2022
© Author(s) 2022. CC BY 4.0 License.

Basic flow fields in our numerical simulation are established on the basis of the ARPS (version 5.3.4). And the filtered continuity and momentum equations including viscous drag force terms of sand particles as well as SCBs are shown as follows (Dupont et al., 2013; Vinkovic et al., 2006):

$$\frac{\partial \tilde{u}_i}{\partial t}+\tilde{u}_j\frac{\partial \tilde{u}_i}{\partial x_j}=-\frac{1}{\bar{\rho}_f}\frac{\partial}{\partial x_i}(\tilde{p}-\nu\frac{\partial \bar{\rho}_f\tilde{u}_j}{\partial x_j})-\frac{\partial \tau_{ij}}{\partial x_j}-\delta_{i3}g(\frac{\tilde{\theta}}{\bar{\theta}}-\frac{c_p}{c_v}\frac{\tilde{p}}{\bar{p}})+\frac{F_i}{\bar{\rho}_f}, \quad (1)$$

where, i = 1, 2 and 3 correspond to the streamwise, spanwise and wall-normal directions (i.e., $x_1 = x,\ x_2 = y,\ x_3 = z,\ u_1 = u,\ u_2 = v,\ u_3 = w$), respectively; $\tilde{u}_i$, $\tilde{p}$ and $\tilde{\theta}$ represent the filtered wind speed, pressure and potential temperature, respectively; v is a damping coefficient of the attenuate acoustic waves; ρ_f is the air density; g is the acceleration of gravity; F_i is the feedback force of sand particles and SCBs; $\delta_{ij}=1$ if $i=j$, otherwise $\delta_{ij}=0$; $\tau_{ij}=\widetilde{u_iu_j}-\tilde{u}_i\tilde{u}_j$ are the SGS (sub-grid-scale) stresses (Smagorinsky, 1963); c_p and c_v are the specific heat of air at constant pressure and volume, respectively.

In order to solve above equations, the SGS stresses can be closed as follows:

$$\tau_{ij}-\frac{1}{3}\tau_{kk}\delta_{ij}=-(C_{sgs}\Delta)^2\frac{1}{\sqrt{2}}\left|\frac{\partial \tilde{u}_i}{\partial x_j}+\frac{\partial \tilde{u}_j}{\partial x_i}\right|(\frac{\partial \tilde{u}_i}{\partial x_j}+\frac{\partial \tilde{u}_j}{\partial x_i}), \quad (2)$$

where Δ is the grid scale; C_{sgs} depends on the Germano subgrid-scale closure method (Germano et al., 1991).

For the governing equations mentioned above, periodic boundary conditions are applied for spanwise direction. The upper and lower boundaries are set as a stress-free condition and a rigid ground condition, respectively. The outlet boundary is used as an

https://doi.org/10.5194/egusphere-2022-714
Preprint. Discussion started: 12 September 2022
© Author(s) 2022. CC BY 4.0 License.

open radiation condition in this paper. The inlet boundary is a given logarithmic profile:

$$\tilde{u}(0, y, z) = (\frac{u_*}{\kappa})\ln(\frac{z}{z_0}). \tag{3}$$

Here k=0.41 is von Kármán constant; z_0=D/30 is the aerodynamic surface roughness (Kok et al., 2012); u_* is the friction speed of inflow. Additionally, the simulation is driven by a constant flow corresponding to the given logarithmic wind profile. In order to accelerate the development of boundary layer flow, LWS method (Lund et al., 1998) are applied to the inlet condition and the recycling plane at x_{ref} =5m (x_{ref}/Lx=12.5% (Inoue and Pullin, 2011), see Fig. 1). The specific method is to re-assign the calculated mean velocity and fluctuation at the recycling plane to the inlet at each fluid time step. There is a similar application in the paper of Xu et al. (2018).

2.2 Movement of sand particles

Saltating particles are moved by the drag force, gravity, electric field force, Magnus force, Saffman force and so on (Murphy and Hooshiari, 1982). In our model, the drag force and gravity are considered, ignoring other minor factors (Kok et al., 2012; Zou et al., 2007). We employ the Lagrangian point-particle method to describe particle motions, and the equations of particles with different sizes in three directions can be expressed as

$$m_p \frac{d^2 x}{dt^2} = \frac{C_D \pi D^2 \rho_f}{8}(\tilde{u} - \frac{dx}{dt})^2 + F_{nx} + F_{sx}, \tag{4}$$

https://doi.org/10.5194/egusphere-2022-714
Preprint. Discussion started: 12 September 2022
© Author(s) 2022. CC BY 4.0 License.

$$m_p \frac{d^2 y}{dt^2} = \frac{C_D \pi D^2 \rho_f}{8} (\tilde{v} - \frac{dy}{dt})^2 + F_{ny} + F_{sy}, \tag{5}$$

$$m_p \frac{d^2 z}{dt^2} = -\frac{\pi g \rho_p D^3}{6} + \frac{C_D \pi D^2 \rho_f}{8} (\tilde{w} - \frac{dz}{dt})^2 + F_{nz} + F_{sz}, \tag{6}$$

where m_p is the mass of sand particles; C_D is the drag coefficient of sand particles (Cheng, 1997). The particle Reynolds number can be expressed as

$$\mathrm{Re}_p = (V_f \rho_p D / \mu)[(\tilde{u} - dx/dt)^2 + (\tilde{v} - dy/dt)^2 + (\tilde{w} - dz/dt)^2]^{1/2}. \tag{7}$$

ρ_p and ρ_f are the density of sand particles and air, respectively; D is the diameter of sand particles; $V_f = 1 - \sum_{k=1}^{k=n} V_P / \Delta V$ is the bulk fraction which is the total sand volumes within grid to the bulk of unit grid; ΔV is the bulk of unit grid; μ is the kinetic viscosity coefficient of air; F_{nx}, F_{sx}, F_{ny}, F_{sy}, F_{nz} and F_{sz} are the normal and tangential force of contact in three directions.

2.3Particle collision

The collision process in the air among the ejection particles is focused in previous models (Carneiro et al., 2013; Huang et al., 2007). In this paper, the "spring-damping" model is used to calculate the contact force when particles collide in the air. And the contact force can be described as follows (Huang et al., 2017):

The normal force of contact is

$$\vec{F}_{n,ij} = \begin{cases} -k_n \zeta_{n,ij} \vec{n}_{ij} - d_n \vec{v}_{n,ij} & , \quad \zeta = \left| \mathrm{R}_i + R_j - \vec{r}_{ij} \right| \\ 0 & , \quad \zeta < 0 \end{cases}. \tag{8}$$

Where, $k_n = 2 \times 10^6$ is the normal stiffness coefficient; ζ is the amount of overlap between particles during contact; R_i and R_j are the radius of particle i and j; $\vec{r}_{ij}$ is

https://doi.org/10.5194/egusphere-2022-714
Preprint. Discussion started: 12 September 2022
© Author(s) 2022. CC BY 4.0 License.

distance vector between particles; $\vec{v}_{n,ij}$ is the normal relative velocity vector. The normal damping coefficient can be expressed as

$$d_n = \sqrt{\frac{4k_n \dfrac{m_i m_j}{m_i + m_j}(\ln \varepsilon)^2}{\pi^2 + (\ln \varepsilon)^2}}. \quad (9)$$

Where, m_i and m_j are the mass of particle i and j, and ε =0.7 is restitution coefficient.

The tangential force of contact is

$$\vec{F}_{t,ij} = \begin{cases} -k_t \zeta_{t,ij} \vec{\tau}_{ij} - d_t \vec{v}_{t,ij} & \left|\vec{F}_{t,ij}\right| \le \dfrac{R_i}{R_j}\left|\vec{F}_{n,ij}\right| \\ -\mu_i \left|\vec{F}_{n,ij}\right| \vec{\tau}_{ij} & \left|\vec{F}_{t,ij}\right| > \dfrac{R_i}{R_j}\left|\vec{F}_{n,ij}\right| \end{cases}. \quad (10)$$

Where, k_t $=2\times10^6$ is the tangential stiffness coefficient; $\zeta_{t,ij}$ is the tangential displacement; $\vec{v}_{t,ij}$ is the tangential relative velocity vector. The tangential damping coefficient can be expressed as

$$d_t = 2\sqrt{\frac{m_i m_j}{m_i + m_j} k_t}. \quad (11)$$

2.4 Splash process

Splash processes not only serve as an indispensable part of the near-surface particle motions, but also relate to the accuracy of emissions during particles upward transport. There are a large number of collisions between particles and the ground. Meanwhile, other particles will be blown up when particles hit the ground, which is referred to as the splash process. If energy-based collision analysis is performed on a single particle, lots of time will be consumed. Therefore, researchers parameterized some key variables in accordance with the characteristics of splash, thereby

https://doi.org/10.5194/egusphere-2022-714
Preprint. Discussion started: 12 September 2022
© Author(s) 2022. CC BY 4.0 License.

simplifying the problem. We assume that there are enough sand and dust particles on the ground to splash when the particles impact the surface. If the particle collides with the bed, we assume the rebound probability as

$$p_{reb} = 0.95(1 - e^{-\lambda v_{imp}}), \tag{12}$$

where v_{imp} is the impact speed, and λ is an empirical parameter in the order of 2 s/m according to the previous study (Anderson et al., 1991). The rebound sand speed is 0.55 times of the impact sand speed, and the rebound angle θ_{reb} is 40° (Zhou et al., 2006). Of course, at a certain speed, some new sand particles will be splashed. The ejection number is

$$\overline{N_{ej}} = n_0\left(1 - \left(A - B\sin\theta_{imp}\right)^2\right)\left(\frac{v_{imp}}{\zeta\sqrt{gd_{mean}}} - 1\right)(e^{\mu_{imp}/C} - D). \tag{13}$$

Where, n_0=0.4, A=0.68, B=0.39, ζ=5, C=0.92, D=1.39 (Huang et al., 2017). θ_{imp} is the impact angle, μ_{imp} is the ratio of impact grain size to the mean size of the bed, and d_{mean} is the mean diameter of the sand particles. The ejection angle θ_{ej} distributes randomly between 50~60° (Rice et al., 1995). The probability density distribution of the initial lifting speed follows

$$p(v_{ej}) = \exp(-v_{ej} / \overline{v_{ej}}) / \overline{v_{ej}}. \tag{14}$$

Where, v_{ej} is the ejection speed and the overbar represents a mean value (Anderson et al., 1991; Werner, 1990). The mean ejection speed can be expressed as (Kok and Renno, 2009)

https://doi.org/10.5194/egusphere-2022-714
Preprint. Discussion started: 12 September 2022
© Author(s) 2022. CC BY 4.0 License.

$$\overline{v_{ej}} = \sqrt{gD_{mean}}\frac{\alpha_{ej}}{a}(1-\exp(-\frac{v_{imp}}{40\sqrt{gD_{mean}}})). \quad (15)$$

Moreover, the sand particles satisfy the periodic boundary condition in the direction of streamwise and spanwise, respectively. Following the idea of Dupont et al. (2013), aerodynamic entrainment did not consider in our model. 10000 initial particles are randomly released in the flow field (Huang, 2020), and the release height should be lower than 0.3 m (Shao and Raupach, 1992). The results of Dupont et al. (2013) showed that the number of released particles does not affect the final results, but only the speed of wind-blwon sand development.

2.5 Parameters and equivalent method of SCBs

According to the experience of laying SCBs in practical engineering (Chang et al., 2000) and the theoretical results of Wang and Zheng (2002), in this paper, the height of SCB (S_h) is set to 10 cm, the side length of a single SCB (S_l) is 100×100 cm, and the side thickness of the SCB (S_n) is set to 10 cm. The diagram of a single SCB is shown in Fig. 1b. Moreover, in order to study the inhibition effect of the laying length of SCBs (represented by N) on aeolian sand erosion, we set N=5~10 m, 5~20 m, 5~30 m in the simulation cases. The diagram of the laying SCBs is shown in Fig. 1a and the main parameters of the SCBs are listed in Table 1.

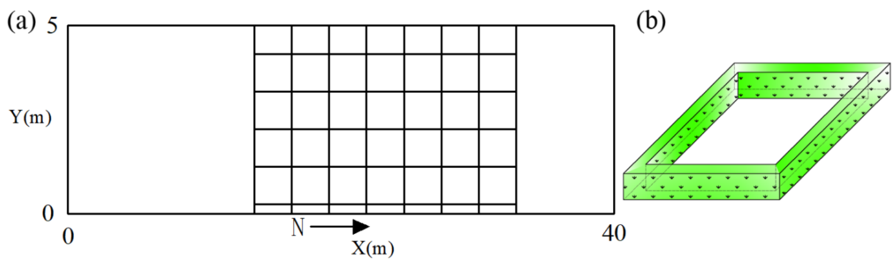

https://doi.org/10.5194/egusphere-2022-714
Preprint. Discussion started: 12 September 2022
© Author(s) 2022. CC BY 4.0 License.

Figure 1. (a) The diagram of the laying SCBs. (b) The diagram of a single SCB.

The SCBs are equivalent to a volume resistance force through the resistance coefficient and leaf area coefficient, that is, the flow in these regions will be subject to additional resistance force, which can be expressed as

$$F_d = -C_d a|U|u_i. \tag{16}$$

Where, C_d is the drag coefficient, a is the leaf area coefficient, and U is the inflow wind speed. In the simulation, the value of C_d is 0.2 according to the parameters of Dupont et al. (2013). Nepf (2012) concluded that when the diameter of vegetation is 4-9 cm, the value of the leaf area coefficient a can reach 20 m^{-1}. Therefore, according to the side thickness of the SCB in this paper, the leaf area coefficient is set as 40 m^{-1}.

Table 1 SCB Parameters

Name	Symbol	Value	Unit
SCB height	S_h	10	cm
SCB side length	S_l	100	cm
SCB side thickness	S_n	10	cm
laying length of SCBs	N	5~10, 5~20, 5~30	m
drag coefficient	C_d	0.2	
leaf area coefficient	a	40	m^{-1}

2.6 Calculation parameters

https://doi.org/10.5194/egusphere-2022-714
Preprint. Discussion started: 12 September 2022
© Author(s) 2022. CC BY 4.0 License.

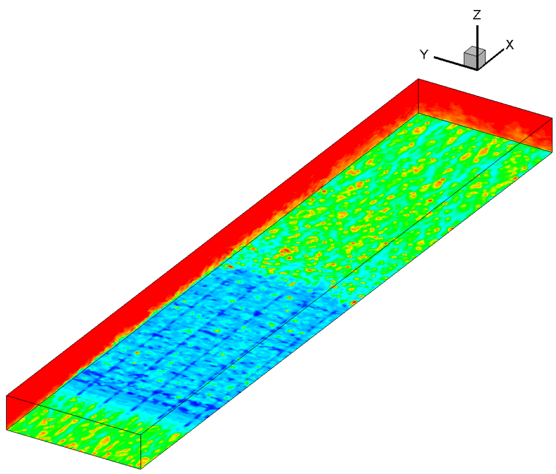

Figure 2. Schematic diagram of three-dimensional wind-blown sand in presence of SCBs.

Wind tunnel experiments conducted by Shao and Raupach (1992) indicated that a complete "overshoot" had more than 10 m in streamwise (Huang et al., 2014; Ma and Zheng, 2011). In Fig. 2, the computational domains are Lx=40 m, Ly=5 m, Lz=2 m in streamwise, spanwise and wall-normal directions, respectively. Field experiments conducted by Baas and Sherman (2005) showed that the mean lateral size of sand streamers is about 0.2 m. In order to capture this structure, the mesh spacing is 0.1 m and 0.1 m in streamwise and spanwise, respectively. Besides, in the near wall region, the logarithmic stretching has been adopted to ensure the precision. The mean and minimum mesh spacing in the vertical direction is 0.025 and 0.005 m, respectively. Therefore, the grids of streamwise, spanwise and vertical directions are $400\times100\times80$, respectively. The sand diameter satisfies the normal distribution: mean diameter equals to 200 μm and the variance is ln(1.2). We first simulate the clean air flow in presence of SCBs for 30 seconds to get fully developed. Then we add the sand

https://doi.org/10.5194/egusphere-2022-714
Preprint. Discussion started: 12 September 2022
© Author(s) 2022. CC BY 4.0 License.

particles in the simulations to develop the sand-laden flow. After the wind-blown sand flow becomes saturated, the simulations last another 20 seconds to do the statistics. The fluid time step Δt_s=0.0002 s, and the particle time step Δt_p=0.00005 s. The density of sand grain is 2650 kg/m^3, and the density of air 1.225kg/m^3. The main calculation parameters are listed in Table 2.

Table 2 Main Simulation Parameters

Name	Symbol	Value	Unit
streamwise computational domain	Lx	40	m
spanwise computational domain	Ly	5	m
wall-normal computational domain	Lz	2	m
fluid time step	Δt_s	0.0002	s
friction wind speed	u_*	0.3, 0.44, 0.6	m/s
particle time step	Δt_p	0.00005	s
sand density	ρ_a	2650	kg/m^3
air density	ρ_f	1.225	kg/m^3
gravity	g	9.81	m/s^2

3. Model validations

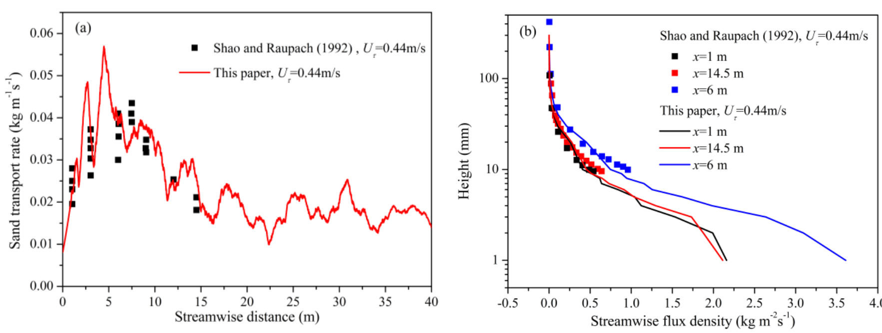

Figure 3. (a) The spatial variation of the streamwise sand transport rate in the sand-laden flow. (b) The streamwise sand transport rate density with the height at the three flow direction positions.

The verification of the flow field part of the program is covered in great detail in our previous works (Huang, 2020). In this section, we will verify the validity of the

https://doi.org/10.5194/egusphere-2022-714
Preprint. Discussion started: 12 September 2022
© Author(s) 2022. CC BY 4.0 License.

model from the following three aspects. Sand transport rate is an important physical quantity in the wind-blown sand, which is the embodiment of the sediment carrying capacity of the flow field (Zheng, 2009). Therefore, without considering the SCBs, we first compare the spatial variation of the sand transport rate in the sand-laden flow with the experimental results of Shao and Raupach (1992). The sand transport rate is calculated according to the formula

$$q = \sum_{z=0}^{z=H} \sum_{y=0}^{y=M} m(x) / \Delta x / \Delta t_s . \tag{17}$$

$m(x)$ represents the sand mass in the range of flow direction x to $x+\Delta x$, and Δx is the grid size in the flow direction. And judge whether the wind-blown sand flow is saturated by the change of the sediment transport at a certain streamwise position. The condition for judging saturation is given by Ma and Zheng (2010). The wind tunnel experimental results of Shao and Raupach (1992) showed that the streamwise sand transport rate increased first, then decreased until it was stable, which is called the "overshoot" phenomenon (Anderson and Haff, 1991; McEwan and Willetts, 1991). Fig. 3a shows the comparison between the simulation results of the sand transport rate along the flow direction with the experimental results of Shao and Raupach (1992) under the same friction wind speed. As can be seen from Fig. 3a, our simulation results also show this phenomenon. However, unlike the other numerical simulation results (Huang et al., 2014; Ma and Zheng, 2011), our sediment transport rate results have an obvious fluctuation characteristic that are not smooth curves, which may be caused by the turbulence intermittency unique to the three-dimensional wind-blown sand model. What's more, we give the distribution results of the streamwise sand transport rate density with the height at the three flow direction positions, which are compared with the experimental results. From Fig. 3b, we can see that the distribution of the streamwise sand transport rate density with the height follows the trend of exponential decline, and the sand transport rate density at x = 6 m is significantly higher than that at x = 1 m and x = 14.5 m, which is consistent with the experimental results of Shao and Raupach (1992). This is because the flow direction of x = 6 m is in the peak region of the "overshoot" phenomenon, while the flow direction of x = 1 m and x = 14.5 m is in the rising region and stable region, respectively. Due to the massive accumulation of sand particles exist near the surface (0-20 mm), thus the concentrations cannot be measured easily. In Fig. 3b, our simulation results can also show that the distribution of the streamwise sand transport rate density with the height below 10 mm still satisfies the trend of exponential decline. However, at a height of 2~3 mm, there is a slight change in this trend, that is, the rate of increase in the sand transport rate density has slowed down, which is not revealed in the experimental results. Due to the limitations of the large eddy simulation, the simulation results near the wall may be distorted, so this part needs to be further verified by the experiments.

https://doi.org/10.5194/egusphere-2022-714
Preprint. Discussion started: 12 September 2022
© Author(s) 2022. CC BY 4.0 License.

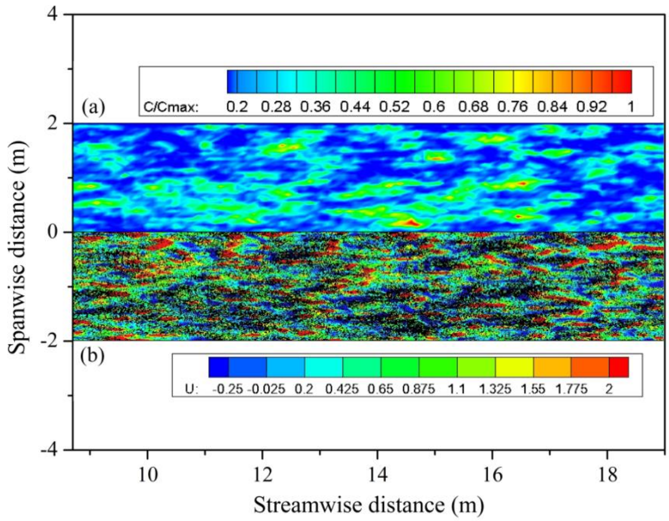

325

326 **Figure 4.** (a) The top view of the sand streamer concentrations, where C represents the particle concentrations, C_{max} represents the maximum particle concentrations. (b) The top view of the whole particle positions and the streamwise velocity diagram of flow field with the height of 0.005 m, and the y coordinates are correspondingly shifted down by 2, where the black dots represent the sand particles, U represents the streamwise wind speed of the sand-laden flow (u_τ=0.3 m/s).

331 Sand streamer, as a natural phenomenon in wind-blown sand, has been widely concerned. Therefore, without considering the SCBs, we then analyze the morphology of sand streamer and its relationship with the flow field. In the meantime, the air-borne particle concentration within a certain area can be calculated as

$$C = \sum_{z=0}^{z=H} \sum_{y=0}^{y=M} \sum_{x=0}^{x=L} m(x) / Lx / Ly / Lz. \quad (18)$$

336 Fig. 4a is the top view of particle-aggregation morphology in the stable stage of sand-laden flow. It can be seen from Fig. 4a that the concentration of sand particles is intermittent in both streamwise and spanwise directions. Moreover, we can see clearly

https://doi.org/10.5194/egusphere-2022-714
Preprint. Discussion started: 12 September 2022
© Author(s) 2022. CC BY 4.0 License.

that the morphological characteristics of sand streamer are consistent with the observations of Baas and Sherman (2005), that is, it is up to a few meters in the streamwise direction and about 0.2 meters in the spanwise direction. Our model can reproduce the "sand streamer" phenomenon in wind-blown sand well. Here, we need to point out that the intermittence of turbulence complicates the particle movement, especially when multiple streamers are connected end to end as well as the concentration is close enough, there will existing the super sand streamers up to tens of meters long. Whether in the sand-laden flow or the other two-phase flows, researchers are generally concerned about the aggregation of particles. We plot the position of particles and the streamwise velocity of flow field in Fig. 4b, and notice that most particles are assembled in the low-speed streaks, which is consistent with the conclusion of the other particle-laden flows (Lee and Lee, 2015; Richter, 2015).

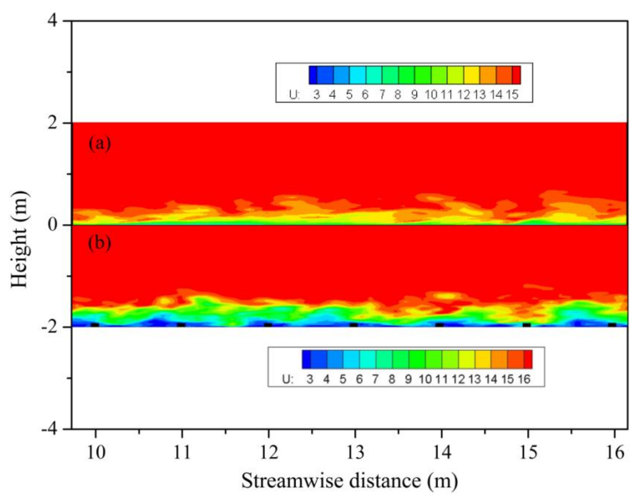

Figure 5. The side view of X-Z plane streamwise velocity before (a) and after (b) containing the SCBs (u_τ=0.6 m/s, N=5~20 m, y=0 m). The y coordinates are correspondingly shifted down by 2

https://doi.org/10.5194/egusphere-2022-714
Preprint. Discussion started: 12 September 2022
© Author(s) 2022. CC BY 4.0 License.

in the case (b).

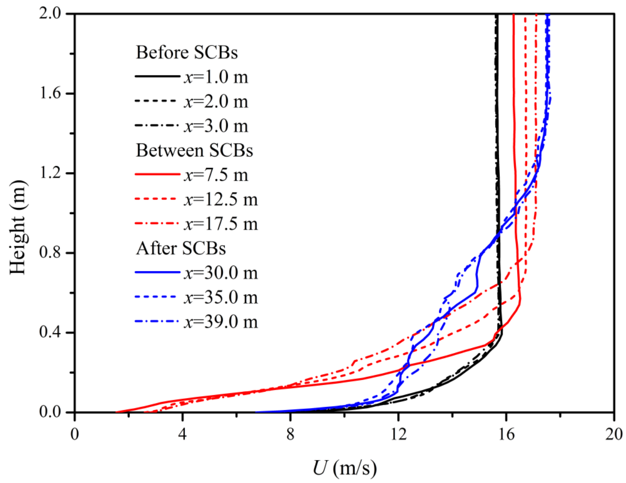

Figure 6. The wind speed profiles of different streamwise positions in the clean air flow containing the SCBs (u_τ=0.6 m/s, N=5~20 m).

Finally, we verify the difference of the velocity profile as well as the surface roughness in the clean air flow with and without the SCBs. In the previous studies, the wind speed and surface roughness near the SCBs were studied well (Dong et al., 2000; Qu et al., 2007; Wang et al., 1999). These works all pointed out that laying the SCBs can effectively increase the surface roughness and reduce the wind speed near the surface, so as to play a role in inhibiting the wind-blown sand and fixing the sand particles. Fig. 5a and 5b are the tangent plane (X-Z plane) of the streamwise wind velocity without and with the SCBs, respectively. It can be seen intuitively that the existence of the SCBs reduces significantly the surface wind speed, and increases the boundary layer thickness of the flow field. In order to reveal the difference quantitatively, we plot the wind speed profiles of different streamwise positions in the

https://doi.org/10.5194/egusphere-2022-714
Preprint. Discussion started: 12 September 2022
© Author(s) 2022. CC BY 4.0 License.

clean air flow containing the SCBs in Fig. 6. The selected positions are x = 1, 2, 3 m in front of the SCBs, x = 7.5, 12.5, 17.5 m in the area containing the SCBs, and x = 30, 35, 39 m behind the SCBs. We can see that the wind speed profiles at the three positions in front of the SCBs are basically the same. In the area containing the SCBs, the existence of the SCBs reduces the surface wind speed and increases the thickness of the boundary layer (equivalent to increasing the surface roughness) as well as the incoming wind speed outside the boundary layer. Moreover, the longer the SCBs are, the thicker the boundary layer will be, and the incoming wind speed outside the boundary layer will also increase more. The flow field behind the SCBs may be complicated by the influence of the attached vortex generated by the SCBs, but the overall trend is the same and the boundary layer thickness remains consistent. These results are qualitatively consistent with the existing conclusions (Dong et al., 2000; Qu et al., 2007; Wang et al., 1999), which indicates that our model has effectively introduced the SCBs module. In the following section, we will reveal more about the influence of the laying length on the wind field and its inhibition effect on the wind-blown sand.

4. Results and Discussion

4.1 The influence of the SCBs on the clean air flow

https://doi.org/10.5194/egusphere-2022-714
Preprint. Discussion started: 12 September 2022
© Author(s) 2022. CC BY 4.0 License.

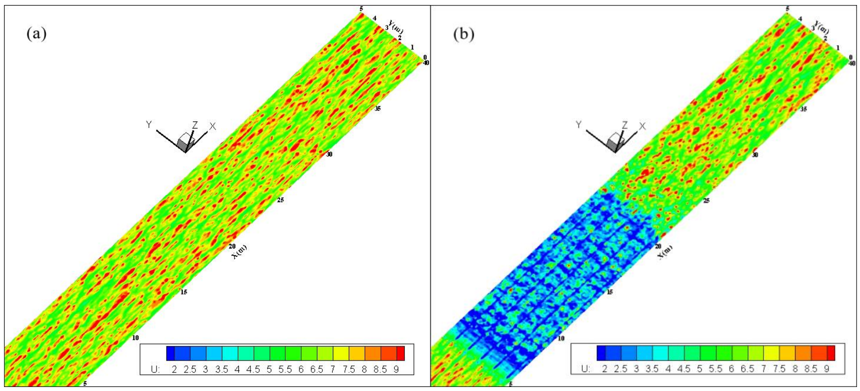

Figure 7. The top view of X-Y plane streamwise velocity without (a) and with (b) the SCBs (z=0.005 m, u_τ=0.6 m/s, N=5~20 m).

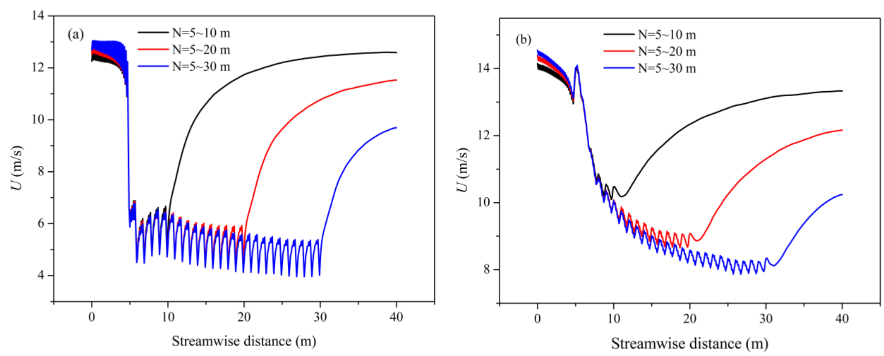

Figure 8. The streamwise wind speed in the clean air flow containing the SCBs at the height of 0.1 m (a) and the height of 0.2 m (b), u_τ=0.6 m/s, N=5~10 m, 5~20 m, 5~30 m.

Fig. 7a and 7b show the presence of the SCBs destroys the original streaks of the clean air flow and decreases the wind speed. The wind speed in the central area of a single SCB is significantly higher than that in the surrounding area, showing a block of velocity distribution characteristics. Although the wind speed behind the SCBs will recover rapidly, there is a significant difference between the newly formed streaks and the original streaks of the flow field, that is, the streamwise scale of the streaks behind

https://doi.org/10.5194/egusphere-2022-714
Preprint. Discussion started: 12 September 2022
© Author(s) 2022. CC BY 4.0 License.

the SCBs is significantly shorter than before. The variation of streamwise wind speed at the different laying length cases (N=5~10 m, 5~20 m, 5~30 m) under the same friction wind speed (u_τ=0.6 m/s) was plotted in Fig. 8, where Fig. 8a corresponds to the wind speed at the height of 0.1 m, and Fig. 8b corresponds to the wind speed at the height of 0.2 m. It can be seen from Fig. 8 that the wind speed in the SCBs decreases in a process of oscillation. And behind the SCBs, the wind speed gradually increases and returns to stability. The trend of wind speed reduction in the SCBs is consistent with the existing experimental results (Xu et al., 1982). The difference is that the reduction process of the wind speed around the SCBs was oscillatory attenuation instead of continuous decrease, which is not revealed in the previous simulation results (Bo et al., 2015). Moreover, when the incoming wind speed is stable, the longer the laying lengths, the lower the wind speed in the stable stage behind SCBs. This is very useful information. On this basis, we can obtain the relationship between the laying length of the SCBs and the wind speed in the stable stage according to an actual situation. For example, reduce the wind speed in the stable stage to the impact threshold or the aerodynamic threshold on both sides of the desert highway, so as to determine the minimum laying length of the SCBs and save the laying cost. This is a potential application of our model and needs to be further verified by the experiments.

4.2 Effect of sand particles on the flow field and its aggregation location

https://doi.org/10.5194/egusphere-2022-714
Preprint. Discussion started: 12 September 2022
© Author(s) 2022. CC BY 4.0 License.

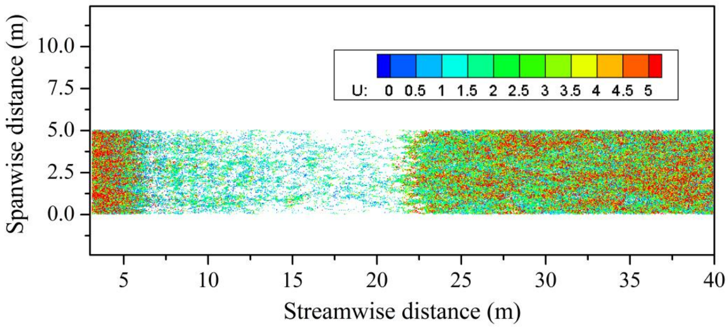

Figure 9. The top view of the particle positions of the wind-blown sand in presence of SCBs, where U represents the speed of the particles (u_τ=0.6 m/s, N=5~20 m).

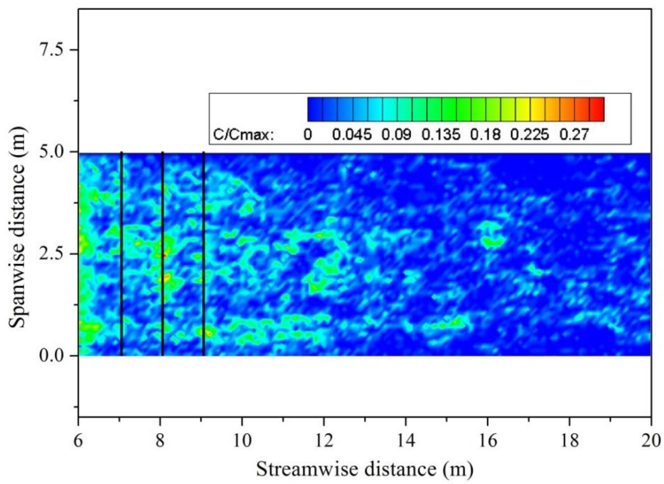

Figure 10. The top view of the sand concentrations in the regions of the SCBs, where C represents the particle concentrations, C_{max} represents the maximum particle concentrations (u_τ=0.6 m/s, N=5~20 m). The black lines represent the schematic diagram of the side of SCBs.

Then, sand particles were added to the clean air flow field in presence of SCBs to fully develop and reach stability. The top view of the particle positions of the wind-blown sand after reaching a stable state is shown in Fig. 9. From Fig. 9, we can see that when the wind-blown sand pass through the SCBs, the particle number

https://doi.org/10.5194/egusphere-2022-714
Preprint. Discussion started: 12 September 2022
© Author(s) 2022. CC BY 4.0 License.

obviously decreases gradually, and the inhibition effect of the SCBs on the wind-blown sand can be visualized. Moreover, the motion of sand particles behind the SCBs returns to a complete wind-blown sand movement. We then plot the sand concentrations of the region in presence of SCBs in Fig. 10. Combining the laying position of the SCBs as well as the corresponding sand concentrations, we can clearly see that the concentration of sand particles near the side of SCBs is higher than that in its central region, which is consistent with the conclusion of Xu et al. (2018). On the one hand, the wind speed near the side of SCBs is low, and the drag force of the sand particles in these areas will be significantly reduced, so that the sand particles will accumulate or deposit in these regions. On the other hand, the wind speed in the central area of every single SCB is significantly higher than that in the surrounding area, so that the sand particles are not easy to gather or fall in these regions. This explains why the side of the SCBs tends to be buried in the sandy land and loses its effect after long working hours.

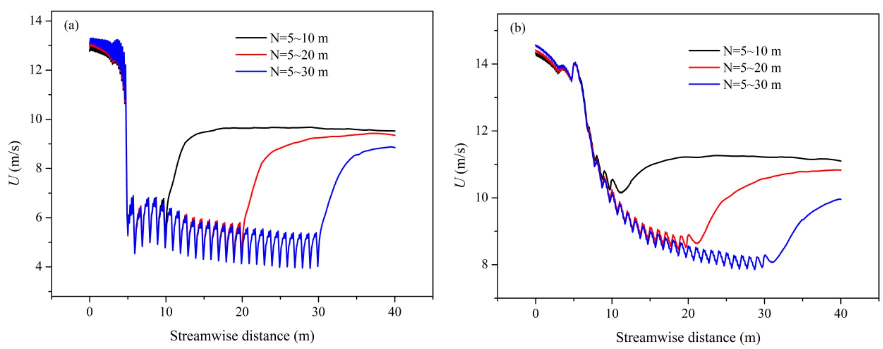

https://doi.org/10.5194/egusphere-2022-714
Preprint. Discussion started: 12 September 2022
© Author(s) 2022. CC BY 4.0 License.

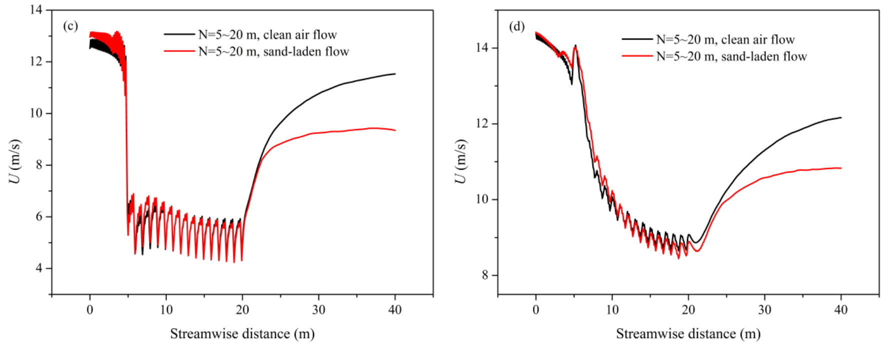

Figure 11. The streamwise wind speed in the sand-laden flow containing the SCBs at the height of 0.1 m (a) and the height of 0.2 m (b), u_τ=0.6 m/s, N=5~10 m, 5~20 m, 5~30 m. The comparison of the streamwise wind speed between the clean air flow and the sand-laden flow at the height of 0.1 m (c) and the height of 0.2 m (d), u_τ=0.6 m/s, N=5~20 m.

Furthermore, we analyze the effect of sand particles on the wind speed in the sand-laden flow. The streamwise wind speed of the sand-laden flow at the different laying length cases (N=5~10 m, 5~20 m, 5~30 m) under the same friction wind speed was plotted in Fig. 11a and 11b. Meanwhile, for the convenience of comparison, the streamwise wind speed under the same laying length (N=5~20 m) in the sand-laden flow and the clean air flow were plotted in Fig. 11c and 11d. Fig. 11a and 11c correspond to the wind speed at a height of 0.1 m, while Fig. 11b and 11d correspond to the wind speed at a height of 0.2 m. From Fig. 11a-d, we can see that the wind speed in the SCBs of the sand-laden flow still decreases in a process of oscillation. The streamwise wind speed behind the SCBs in the sand-laden flow is significantly lower than that in the clean air flow. Obviously, the presence of sand particles indeed reduces the wind speed. However, the change of wind speed in the SCBs between the

https://doi.org/10.5194/egusphere-2022-714
Preprint. Discussion started: 12 September 2022
© Author(s) 2022. CC BY 4.0 License.

sand-laden flow and the clean air flow is not obvious, because there are fewer sand particles in the SCBs than behind the SCBs, which has less effect on the overall wind speed.

4.3 Effect of laying length on the sand transport rate

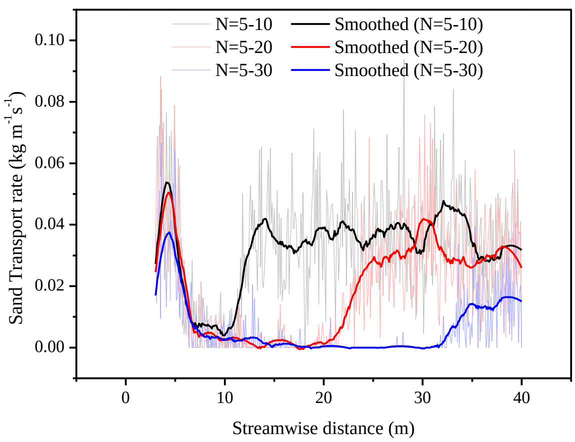

Figure 12. The streamwise sand transport rate in the different laying length cases (u_τ=0.6 m/s, N=5~10 m, 5~20 m, 5~30 m). Dark lines are the result of smoothing.

Here, the effect of the different laying length cases (N=5~10 m, 5~20 m, 5~30 m) on the sand transport rate under the same friction wind speed was plotted in Fig. 12. It can be seen from Fig. 12 that the sand transport rate in the SCBs is very low, and with the increase of the laying length, the sand transport rate in the SCBs will be lower and lower. In the case of N=5~30 m, we can even see that the sand transport rate in some regions has been reduced to zero. Therefore, this result once again shows that the laying length of the SCBs can be optimized, and we can reduce the laying cost while keep the effect of the SCBs unchanged. Especially on both sides of the desert highway,

https://doi.org/10.5194/egusphere-2022-714
Preprint. Discussion started: 12 September 2022
© Author(s) 2022. CC BY 4.0 License.

our model can give the minimum laying length according to the actual parameters. At the same time, we notice that the sand transport rate will increase rapidly and then reach to stable state behind the SCBs. And it is obvious that when N=5~30 m, the value of sand transport rate at the stable stage behind the SCBs is significantly lower than the other results of N=5~10 m and N=5~20 m. We also notice that the longer the laying lengths, the lower the sand transport rate in the stable stage behind the SCBs. This result is corresponding to the result of Fig. 8. Our results indicate that when the sandy land is wide, the discontinuous laying method can be considered. That is, determine the minimum laying length first, and then determine the distance between each minimum laying length as required. In this way, the sand transport rate can be reduced in sections. This is another potential application of our model.

4.4 Particle positions under different friction wind speeds

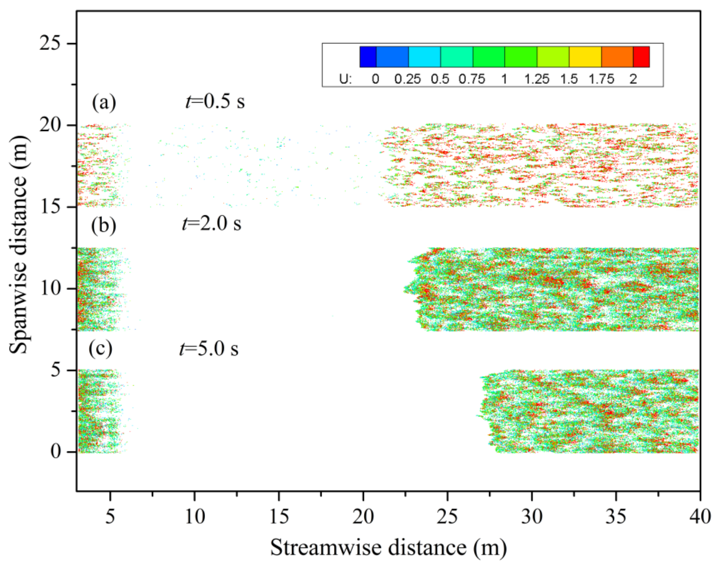

Figure 13. The top view of the particle positions of the wind-blown sand in presence of SCBs at

https://doi.org/10.5194/egusphere-2022-714
Preprint. Discussion started: 12 September 2022
© Author(s) 2022. CC BY 4.0 License.

the time t=0.5 s (a), t=2.0 s (b), t=5.0 s (c), where U represents the speed of the particles (u_τ=0.3 m/s, N=5~20 m). The y coordinates are correspondingly shifted up by 7.5 per case.

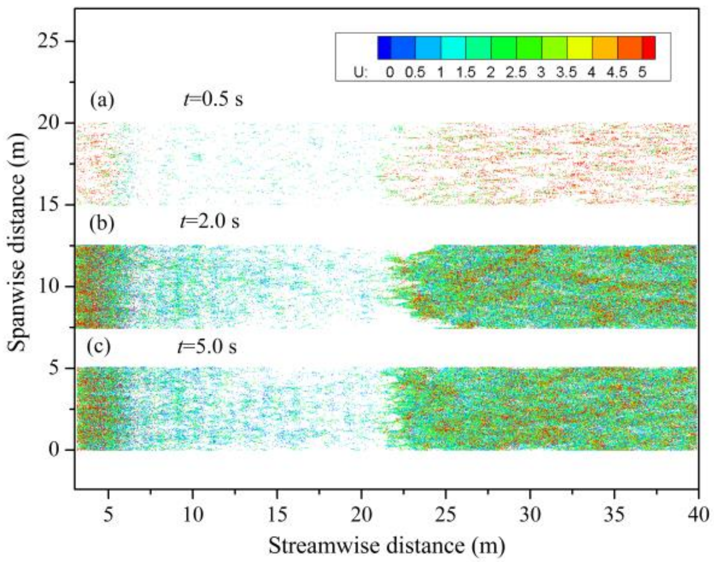

Figure 14. The top view of the particle positions of the wind-blown sand in presence of SCBs at the time t=0.5 s (a), t=2.0 s (b), t=5.0 s (c), where U represents the speed of the particles (u_τ=0.6 m/s, N=5~20 m). The y coordinates are correspondingly shifted up by 7.5 per case.

The above analysis is based on the calculation case when the friction wind speed is 0.6 m/s, and the sand particles can easily penetrate the SCBs when the wind speed is large. When the friction wind speed is small, the inhibition effect of the SCBs on wind-blown sand will become more obvious, and the movement behavior of sand particles will become different. We plot the top view of the particle positions at different moments (t=0.5 s, 2 s, 5 s) when the friction wind speed is 0.3m/s and 0.6m/s in Fig. 13 and Fig. 14, respectively. The time t in Fig. 13 and Fig. 14 counts from the moment sand particles are added. The results show that when the wind speed

https://doi.org/10.5194/egusphere-2022-714
Preprint. Discussion started: 12 September 2022
© Author(s) 2022. CC BY 4.0 License.

is small, the sand particles cannot penetrate the SCBs. There is no obvious sand movement in the SCBs, and the stable wind-blown sand cannot be formed behind the SCBs. With the passage of time, the wind-blown sand behind the SCBs will gradually disappear. It is worth pointing out that aerodynamic entrainment is not considered in our model. This is a strong limitation of our model to simulate wind erosion in presence of SCBs. Therefore, a more reasonable situation is that when the wind speed behind the SCBs returns to the fluid threshold, this part of the wind-blown sand should still develop. When the wind speed is relatively small, on the one hand, the sand particles cannot completely penetrate the regions of the SCBs, and then cannot continuously provide the impact particles to form the wind-blown sand behind the SCBs. On the other hand, the SCBs affect the surface wind speed behind it, thus also affecting the continuous formation of the wind-blown sand. When the wind speed is relatively large, the sand particles can penetrate the SCBs. And with the increase of the laying length, although the inhibition effect on wind-blown sand is more obvious, the stable wind-blown sand will still be formed behind the SCBs. We think that when the laying length of the SCBs is fixed, whether the wind speed will decrease below the impact threshold or the fluid threshold is the key to determine whether the sand particles can penetrate the SCBs and form stable wind-blown sand behind the SCBs. In order to present this phenomenon more clearly, we have animated this process, as shown in the supplementary materials (Video 1 and Video 2). In the actual anti-desertification projects, the minimum laying length of the SCBs can be determined by our model according to the local maximum friction wind speed, which

https://doi.org/10.5194/egusphere-2022-714
Preprint. Discussion started: 12 September 2022
© Author(s) 2022. CC BY 4.0 License.

is very meaningful.

5. Conclusions and outlook

In this paper, a three-dimensional wind-blown sand coupling model in presence of SCBs was established. The model was verified from the following aspects: (1) spatial distribution of sand transport rate; (2) morphological characteristics of sand streamer from the instantaneous fields; (3) changes in the thickness of the boundary layer before and after the SCBs. From this model, the inhibition effect of SCBs on wind-blown sand was studied qualitatively, and the sensitivity of aeolian sand erosion to the laying length was investigated. The results showed that the wind speed in the SCBs of the clean air flow or the sand-laden flow both decreases in a process of oscillation, which has not been revealed by the previous researches. Moreover, the longer the laying lengths of the SCBs, the lower the wind speed in the stable stage behind SCBs, and the lower the sand transport rate, which may provide the theoretical support for the minimum laying length of SCBs in anti-desertification projects. More importantly, we found that the concentration of sand particles near the side of SCBs is higher than that in its central region, which is consistent with the previous research. This explains why the boundary of the SCBs tends to be buried in the sandy land and loses its effect after long working hours. Our results also indicated that whether the wind speed will decrease below the impact threshold or the fluid threshold is the key factor affecting whether sand particles can penetrate the SCBs and form stable wind-blown sand behind the SCBs under the same conditions. Although our model has been able to reveal the inhibition effect of the SCBs on wind-blown sand, there

© Author(s) 2022. CC BY 4.0 License.

are still some aspects to be improved in the future, such as the aerodynamic entrainment, particle deposition on the SCB, and the collision between the sand particles and the SCBs. And the size of the SCB used in our model is fixed. In the future work, we plan to analyze the effect of different height and width of the SCB on the aeolian sand erosion and discuss the reasons for the difference in heights between SCB and other obstacles, such as sand fence. Another aspect worth noting is that some additional factors such as terrain, surface roughness will affect the effect of the SCBs in the anti-desertification project, so the influence of these factors should be considered in the future. The significance of our work is to analyze some results which seemingly simple but lack of theoretical basis from the perspective of turbulence through this model.

Acknowledgments

This research was supported by grants from the National Natural Science Foundation of China (Grant number 12002119), Opening Foundation of MOE Engineering Research Center of Desertification and Blown-sand Control, Beijing Normal University (2021-B-4). The author expresses sincere appreciation to the supports. The author would like to thank the Center for Analysis and Prediction of Storms (CAPS) at the University of Oklahoma for providing the original ARPS code.

Code and Data availability. All relevant code and data used to generate the

https://doi.org/10.5194/egusphere-2022-714
Preprint. Discussion started: 12 September 2022
© Author(s) 2022. CC BY 4.0 License.

figures in this paper can be accessed using the following email: hjhuang@usst.edu.cn.

Competing interests. The authors declare that there are no competing interests

Author contributions. HJ performed the programming, analyzed the results, and wrote the paper.

Video supplement. Video 1 and Video 2 can be downloaded at the following link: https://doi.org/10.5281/zenodo.6937805

References

Anderson, R. S. and Haff, P.: Wind modification and bed response during saltation of sand in air, Acta Mech. Supp. 1, 21-51, 1991.

Anderson, R. S., Sørensen, M., and Willetts, B. B.: A review of recent progress in our understanding of aeolian sediment transport, Acta Mech. Supp. 1, 1-19, 1991.

Baas, A. C. W. and Sherman, D.: Formation and behavior of aeolian streamers, J. Geophys. Res. Earth Surf. 110(F3) , 2005.

Bitog, J., Lee, I. B., Shin, M. H., Hong, S. W., Hwang, H. S., Seo, I. H., Yoo, J. I., Kwon, K. S., Kim, Y. H., and Han, J. W.: Numerical simulation of an array of fences in Saemangeum reclaimed land, Atmos. Environ. 43(30), 4612-4621, 2009.

Bo, T. L., Ma, P., and Zheng, X. J.: Numerical study on the effect of semi-buried straw checkerboard sand barriers belt on the wind speed, Aeolian Res. 16, 101-107, 2015.

Bouvet, T., Wilson, J., and Tuzet, A.: Observations and modeling of heavy particle deposition in a windbreak flow, J. Appl. Meteorol. Climatol. 45(9), 1332-1349, 2006.

Carneiro, M. V., Araújo, N. A., Pähtz, T., and Herrmann, H. J.: Midair collisions enhance saltation, Phys. Rev. Lett. 111(5), 058001, 2013.

Chang, Z., Zhong, S., Han, F., and Liu, H.: Research of the suitable row spacing on clay barriers and straw barriers, J. Desert Res. 20(4), 455-457, 2000.

Chen, B., Cheng, J., Xin, L., and Wang, R.: Effectiveness of hole plate-type sand barriers in reducing aeolian sediment flux: Evaluation of effect of hole size, Aeolian Res. 38, 1-12, 2019.

https://doi.org/10.5194/egusphere-2022-714
Preprint. Discussion started: 12 September 2022
© Author(s) 2022. CC BY 4.0 License.

Cheng, J. J. and Xue, C. X.: The sand-damage-prevention engineering system for the railway in the desert region of the Qinghai-Tibet plateau, J. Wind Eng. Ind. Aerodyn. 125, 30-37, 2014.

Cheng, J. J., Lei, J. Q., Li, S. Y., and Wang, H. F.: Disturbance of the inclined inserting-type sand fence to wind-sand flow fields and its sand control characteristics, Aeolian Res. 21, 139-150, 2016.

Cheng, N. S.: Simplified settling velocity formula for sediment particle, J. Hydraul. Eng. 123(2), 149-152, 1997.

Dai, Y., Dong, Z., Li, H., He, Y., Li, J., and Guo, J.: Effects of checkerboard barriers on the distribution of aeolian sandy soil particles and soil organic carbon, Geomorphology 338, 79-87, 2019.

Dong, Z., Fryrear, D., and Gao, S.: Modeling the roughness effect of blown-sand-controlling standing vegetation in wind tunnel, J. Desert Res. 20(3), 260-263, 2000.

Dupont, S., Bergametti, G., and Simoëns, S.: Modeling aeolian erosion in presence of vegetation, J. Geophys. Res. Earth Surf. 119(2), 168-187, 2014.

Dupont, S., Bergametti, G., Marticorena, B., and Simoëns, S.: Modeling saltation intermittency, J. Geophys. Res. Atmos. 118(13), 7109-7128, 2013.

Germano, M., Piomelli, U., Moin, P., and Cabot, W. H.: A dynamic subgrid-scale eddy viscosity model, Phys. Fluids A: Fluid Dyn. 3(7), 1760-1765, 1991.

Hatanaka, K. and Hotta, S.: Finite element analysis of air flow around permeable sand fences, Int. J. Numer. Methods Fluids 24(12), 1291-1306, 1997.

Huang, H. J., Bo, T. L., and Zhang, R.: Exploration of splash function and lateral velocity based on three-dimensional mixed-size grain/bed collision, Granul. Matter 19(4), 73, 2017.

Huang, H. J., Bo, T. L., and Zheng, X. J.: Numerical modeling of wind-blown sand on Mars, Eur. Phys. J. E 37(9), 80, 2014.

Huang, H. J.: Modeling the effect of saltation on surface layer turbulence, Earth Surf. Proc. Land. 45(15), 3943-3954, 2020.

Huang, N. and Wang, Z. S.: The formation of snow streamers in the turbulent atmosphere boundary layer, Aeolian Res. 23, 1-10, 2016.

Huang, N., Xia, X., and Tong, D.: Numerical simulation of wind sand movement in straw checkerboard barriers, Eur. Phys. J. E 36(9), 99, 2013.

Huang, N., Zhang, Y., and D'Adamo, R.: A model of the trajectories and midair collision probabilities of sand particles in a steady state saltation cloud, J. Geophys. Res. Atmos. 112(D8) , 2007.

Inoue, M. and Pullin, D.: Large-eddy simulation of the zero-pressure-gradient turbulent boundary layer up to Re_{θ}= O (10^{12}), J. Fluid Mech. 686, 507-533, 2011.

Kok, J. F. and Renno, N. O.: A comprehensive numerical model of steady state saltation (COMSALT), J. Geophys. Res. Atmos. 114(D17), 2009.

Kok, J. F., Parteli, E. J., Michaels, T. I., and Karam, D. B.: The physics of wind-blown sand and dust, Rep. Prog. Phys. 75(10), 106901, 2012.

Li, B. and Sherman, D. J.: Aerodynamics and morphodynamics of sand fences: A review, Aeolian Res. 17,33-48, 2015.

Li, B. W., Zhou, X. J., Huang, P. Z., Xu, X. W., Wang, Z. J., and Zhang, C. M.: Wind-Sand Damage and Its Control at Shaquanzi Section of Lan-xin Railway, Arid Zone Res. 15(4), 47-52, 1998.

© Author(s) 2022. CC BY 4.0 License.

Li, G., Wang, Z., and Huang, N.: A Snow Distribution Model Based on Snowfall and Snow Drifting Simulations in Mountain Area, J. Geophys. Res. Atmos. 123(14), 7193-7203, 2018.

Li, X., Xiao, H., He, M., and Zhang, J.: Sand barriers of straw checkerboards for habitat restoration in extremely arid desert regions, Ecol. Eng. 28(2), 149-157, 2006.

Lima, I. A., Araújo, A. D., Parteli, E. J., Andrade, J. S., and Herrmann, H. J.: Optimal array of sand fences, Sci. Rep. 7, 45148, 2017.

Lima, I. A., Parteli, E. J., Shao, Y. P., Andrade, J. S., Herrmann, H. J., and Araújo, A. D.: CFD simulation of the wind field over a terrain with sand fences: Critical spacing for the wind shear velocity, Aeolian Res. 43, 100574, 2020.

Liu, L. and Bo, T. L.: Effects of checkerboard sand barrier belt on sand transport and dune advance, Aeolian Res. 42, 100546, 2020.

Lund, T. S., Wu, X. H., and Squires, K. D.: Generation of turbulent inflow data for spatially-developing boundary layer simulations, J. Comput. Phys. 140(2), 233-258, 1998.

Ma, G. S. and Zheng, X. J.: The fluctuation property of blown sand particles and the wind-sand flow evolution studied by numerical method, Eur. Phys. J. E 34(5), 54, 2011.

McEwan, I. and Willetts, B.: Numerical model of the saltation cloud, Acta Mech. Supp. 1, 53-66, 1991.

Murphy, P. J. and Hooshiari, H.: Saltation in water dynamics, J. Hyd. Div. 108(11), 1251-1267, 1982.

Nepf, H. M.: Flow and transport in regions with aquatic vegetation, Annu. Rev. Fluid Mech. 44, 123-142, 2012.

Qiu, G. Y., Lee, I. B., Shimizu, H., Gao, Y., and Ding, G.: Principles of sand dune fixation with straw checkerboard technology and its effects on the environment, J. Arid. Environ. 56(3), 449-464, 2004.

Qu, J., Zu, R., Zhang, K., and Fang, H.: Field observations on the protective effect of semi-buried checkerboard sand barriers, Geomorphology 88(1-2), 193-200, 2007.

Rice, M. A., Willetts, B. B., and McEwan, I.: An experimental study of multiple grain-size ejecta produced by collisions of saltating grains with a flat bed, Sedimentology 42(4), 695-706, 1995.

Santiago, J., Martin, F., Cuerva, A., Bezdenejnykh, N., and Sanz-Andres, A.: Experimental and numerical study of wind flow behind windbreaks, Atmos. Environ. 41(30), 6406-6420, 2007.

Shao, Y. P. and Raupach, M.: The overshoot and equilibration of saltation, J. Geophys. Res. Atmos. 97(D18), 20559-20564, 1992.

Smagorinsky, J.: General circulation experiments with the primitive equations: I. The basic experiment, Mon. Weather Rev. 91(3), 99-164, 1963.

Vinkovic, I., Aguirre, C., Ayrault, M., and Simoëns, S.: Large-eddy simulation of the dispersion of solid particles in a turbulent boundary layer, Bound.-Layer Meteor. 121(2), 283, 2006.

Wang, X., Chen, G., Han, Z., and Dong, Z.: The benefit of the prevention system along the desert highway in Tarim Basin, J. Desert Res. 19(2), 120-127, 1999.

Wang, X., Zhang, C., Hasi, E., and Dong, Z.: Has the Three Norths Forest Shelterbelt Program solved the desertification and dust storm problems in arid and semiarid China?, J. Arid. Environ. 74(1), 13-22, 2010.

Wang, X.: Discussion of sand hazard control along the Wu-Ji railway line, J. Desert Res. 16(2), 204-206, 1996.

Wang, Z. T. and Zheng, X. J.: A Simple Model for Calculating Measurements of Straw

https://doi.org/10.5194/egusphere-2022-714
Preprint. Discussion started: 12 September 2022
© Author(s) 2022. CC BY 4.0 License.

Checkerboard Barriers, J. Desert Res. 22(3), 229-232, 2002.

Werner, B.: A steady-state model of wind-blown sand transport, J. Geol. 98(1), 1-17, 1990.

Xu, B., Zhang, J., Huang, N., Gong, K., and Liu, Y.: Characteristics of turbulent aeolian sand movement over straw checkerboard barriers and formation mechanisms of their internal erosion form, J. Geophys. Res. Atmos. 123(13), 6907-6919, 2018.

Xu, J. L., Pei, Z. Q., and Wang, R. H.: Exploration of the width of the semi-buried straw checkerboard sand barriers belt, Chin. Desert 2(3), 16-23, 1982.

Xu, X., Hu, Y., and Pan, B.: Analysis of the protective effect of various measures of combating drifting sand on the Tarim Desert Highway, Arid Zone Res. 15(1), 21-26, 1998.

Xue, M., Droegemeier, K. K., and Wong, V.: The Advanced Regional Prediction System (ARPS)-A multi-scale nonhydrostatic atmospheric simulation and prediction model. Part I: Model dynamics and verification, Meteorol. Atmos. Phys. 75(3-4), 161-193, 2000.

Xue, M., Droegemeier, K. K., Wong, V., Shapiro, A., Brewster, K., Carr, F., Weber, D., Liu, Y., and Wang, D.: The Advanced Regional Prediction System (ARPS)-A multi-scale nonhydrostatic atmospheric simulation and prediction tool. Part II: Model physics and applications, Meteorol. Atmos. Phys. 76(3-4), 143-165, 2001.

Xue, M., Droegemeier, K., Wong, V., Shapiro, A., and Brewster, K.: Advanced Regional Prediction System (ARPS) version 4.0 user's guide, Center for Analysis and Prediction of Storms, University of Oklahoma, 380, 1995.

Yang, A.: Closing sandy land to establish vegetation along a desert railway line, J. Desert Res.15(3), 308-311, 1995.

Zhang, C., Li, Q., Zhou, N., Zhang, J., Kang, L., Shen, Y., and Jia, W.: Field observations of wind profiles and sand fluxes above the windward slope of a sand dune before and after the establishment of semi-buried straw checkerboard barriers, Aeolian Res. 20, 59-70, 2016.

Zhang, K. C., Qu, J. J., Liao, K. T., Niu, Q. H., and Han, Q. J.: Damage by wind-blown sand and its control along Qinghai-Tibet Railway in China, Aeolian Res. 1(3-4), 143-146, 2010.

Zhang, S., Ding, G. D., Yu, M. H., Gao, G. L., Zhao, Y. Y., Wu, G. H., and Wang, L.: Effect of straw checkerboards on wind proofing, sand fixation, and ecological restoration in shifting Sandy Land, Int. J. Environ. Res. Public Health 15(10), 2184, 2018.

Zheng, X. J.: Mechanics of wind-blown sand movements, Springer Science & Business Media, 2009.

Zhou, Y. H., Li, W. Q., and Zheng, X. J.: Particle dynamics method simulations of stochastic collisions of sandy grain bed with mixed size in aeolian sand saltation, J. Geophys. Res. Atmos. 111(D15) , 2006.

Zou, X. Y., Cheng, H., Zhang, C. L., and Zhao, Y. Z.: Effects of the Magnus and Saffman forces on the saltation trajectories of sand grain, Geomorphology 90(1-2), 11-22, 2007.